ORIGINAL ARTICLE

Open Access

Simulation and Experimental Research on Liquid Spreading in a Wire-Sawn Kerf

Lin Lin[1] and Hui Huang[1*]

Abstract

The significance of liquids in abrasive wire sawing has been demonstrated in several studies. However, the performance of its spreading behavior is limited by the current development trend, where the wafer has a larger area and the kerf is narrower. Moreover, there are very few studies on the liquid spreading behavior in wire-sawn kerfs. Therefore, a 3D CFD (computational fluid dynamics) model is presented in this paper and used to simulate the liquid spreading behavior in a kerf based on a VOF (volume of fluid) method with a CSF (continuum surface force) model, which is used to simulate multiphase flow, and an empirical correlation for characterizing the liquid dynamic contact angle using UDF (user defined functions). Subsequently, parametric simulations are performed on the kerf area, kerf width, liquid viscosity, liquid surface tension, and liquid velocity at the inlet area of the kerf, and verification experiments are conducted to determine the validity of the simulation model. From the simulation and experimental results, three typical liquid spreading regimes that exhibit different effects on wire sawing in the kerfs are found, and their limiting conditions are identified using non-dimensional analysis. Subsequently, a prediction model is proposed for the liquid spreading regime based on a set of Weber and Capillary numbers. For wire sawing, an increase in the wafer area does not change the liquid spreading regime in the kerf; however, a reduction in the kerf width significantly hinders the liquid spreading behavior. Thereby, the spreading regime can be effectively converted to facilitate wire sawing by adjusting the physical properties and supply conditions of the liquid.

Keywords Spreading regime, Kerf, CFD, Non-dimensional analysis, Prediction model

1 Introduction

Abrasive wire sawing technology has been widely applied in wafer production in the semiconductor and photovoltaic industry. Since the 1990s, multi-wire slurry sawing (MWSS) has been applied in slicing silicon ingots owing to its high throughput, smaller kerf loss, and ability to slice large-sized ingots [1–3]. Recently, diamond wire sawing (DWS) was promoted and achieved industrial status owing to its efficient material removal [4, 5]. In abrasive wire sawing, the cutting liquid is directly sprayed onto the kerf or onto a high-speed moving (5–30 m/s)

wire web, which then carries it into the sawing channel, as shown in Figure 1(a), (b). Here, the significance of the liquid should not be underestimated owing to the nature of its main functions: lubrication, cooling, and chip removal [6, 7]. Particularly, for MWSS, the cutting fluid is used to carry abrasive particles into the sawing channel to achieve material removal.

Considerable research efforts have been devoted to the liquid behavior during abrasive wire sawing owing to its indispensable role. Thus far, majority of the studies have focused on MWSS because of its earlier development, which dates back to when Bhagavat et al. [8] proposed a 2D model for simulating the EHD (elastohydrodynamic) interaction between wire and slurry. They assumed that the flow is incompressible, steady, and laminar, and used the finite element method to analyze the slurry film thickness and pressure distribution. Moreover,

*Correspondence:
Hui Huang
huanghuihh@hotmail.com
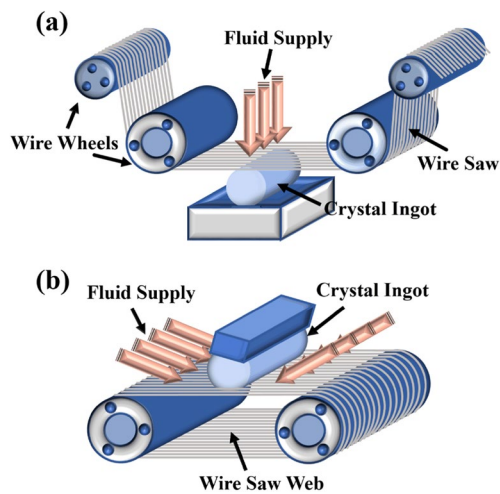[1] State Key Institute of Manufacturing Engineering, Huaqiao University, Xiamen 361021, China

Figure 1 Two main liquid supply modes in abrasive wire sawing: (**a**) Spraying into the kerf, (**b**) Spraying onto a moving wire web

Möller et al. [1] also presented a 2D model for analyzing the EHD behavior of slurry, and several other studies by Bhagavat et al. [8] and Yang et al. [9] have addressed the abrasive behavior of slurry and clarified the prominent impact of the liquid film thickness and pressure distribution on material removal. Furthermore, the significance of the coolant liquid on the thermal environment of wire sawing has also been demonstrated using finite element simulations [10–12].

Although it is not clearly stated, in all the above studies, it is acquiesced that the liquid can enter the sawing channel and remain in a continuous and saturated state. However, a crucial question is overlooked: Whether and how the liquid can enter the sawing area. Therefore, Ishikawa et al. [13] observed the formation of the air layer in the sawing channel, and Nassauer et al. [14] observed the phenomenon of emerging and collapsing micro bubbles in the sawing experiments. Based on these, it was confirmed that there is air in the sawing channel and the liquid is not saturated, which may prevent the liquid from performing its function and result in dry cutting.

Recently, advances in fabrication have resulted in the development of abrasive wire sawing technology to produce larger wafer diameters (from 2 inches to 12 inches) and smaller wire diameters with a lower kerf loss (the current minimum wire diameter is up to 60 μm). This trend promotes the use of a larger sawing kerf area and narrower kerf width in the sawing process. The complex fluid environment at small scales creates entirely new challenges to the entering-spreading behavior of the liquid in the kerf. Nevertheless, for abrasive wire sawing, neither the entering-spreading behavior of the liquid nor the introduction of air has been explicitly represented,

and the liquid supply mode involving direct spraying on the kerf has not been investigated. Moreover, most of the abovementioned studies employ 2D models for simulation, which have inevitable limitations when simulating actual conditions.

In this paper, a 3D CFD model is constructed to simulate the liquid spreading behavior in a kerf, and parametric simulations are performed on the kerf area, kerf width, liquid viscosity, liquid surface tension, and liquid velocity at the kerf inlet area. Furthermore, the validity of the simulation model is verified using experiments.

2 Simulation and Experimental Methodology

This paper aims to investigate the liquid spreading behavior in a kerf, focusing on a liquid supply mode involving direct spraying into the kerf. To simplify the model, the single wire sawing of a sapphire ingot is taken as an example.

2.1 Simulation Model and Boundary Condition

For the physical phenomenon of interest, a series of 3D geometry models are built in different dimensions for parametric simulation (the geometric dimensions of the models are shown in Table 4, see Appendix), and their structural features are shown in Figure 2. As shown in Figure 2(a), the calculation domain is a cuboid, and the inlet, a square orifice of 4×4 mm^2, is set at the center of its top. In the calculation domain, an ingot model, is built 15 mm below the orifice to represent the nozzle position during general sawing. To reduce computational load, the ingot model was simplified to a thickness of 2 mm, and a kerf was processed at the central section of the ingot (Figure 2(a)). Moreover, as presented in Figure 2(d), the sawing area on the kerf surface is simplified to a flat area without the sawing wire.

The geometric models are then meshed into structured hexahedral grids, as shown in Figure 2(b), and local mesh densification is conducted on the ingot and kerf walls, as shown in Figure 2(c). Furthermore, grid size independence is performed to enhance the accuracy and efficiency of the calculation. When the total number of the grid nodes in the model is greater than 2.2×10^4, and the smallest grid volume is less than 2.3×10^{-12} mm^3, the simulation results do not have any significant differences.

The boundary conditions for simulation are shown in Table 1. All walls are assumed to be uniform sandgrain surfaces with certain roughness heights K_s (the determination of the K_s depends on the measured surface roughness). In addition, the operating pressure is 101325 Pa, the gravitational acceleration g is 9.8 m/s^2, and v_0 is the inlet velocity.
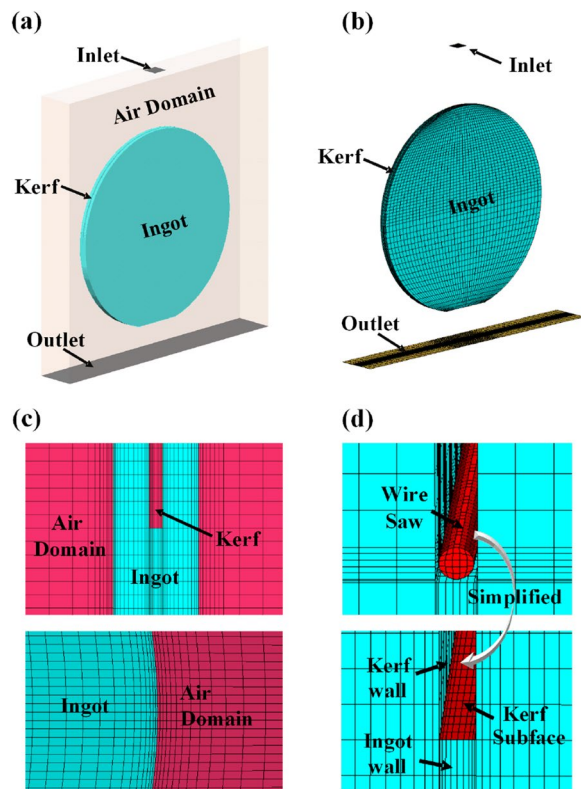
Figure 2 Geometric model and grids: (**a**) Calculation domain and geometric model, (**b**) Grid of the ingot with a kerf, (**c**) Local mesh densification at the ingot and kerf walls, (**d**) Simplification of the sawing area

Figure 3 Experimental setup

2.2 Experimental Setup

The experimental setup (see Figure 3) consists of the following parts: (a) pump, (b) precision valve, (c) float flowmeter, (d) 3D printing nozzle (with a 4 mm×4 mm square outlet), (e) liquid recovery tank, (f) three-axis linkage platform, and (g) high-speed camera (Phantom/V2511). Parts (a)–(d) are connected using water pipes and are located in the liquid recovery tank for flow control and recovery. Additionally, a three-axis linkage platform is fixed at the bottom of the tank, and a 2-inch ingot with a sawn kerf is fixed on the platform (the sawing parameters are shown in Table 5, see Appendix).

The experimental device was simplified based on a diamond wire sawing machine (JXQ-1201) liquid supply system, but the actual sawing process was not considered. Furthermore, various physical parameters were measured and controlled in the experiment to verify the consistency of the experimental and simulated boundary conditions. These include the dimensions of the ingot and its kerf, and the nozzle size (see Table 2) for use in the simula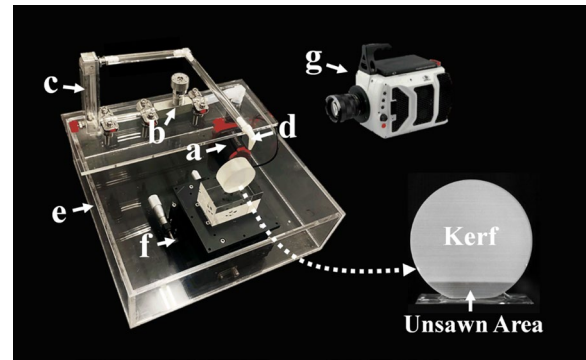tion. In addition, the position of the ingot was adjusted using a three-axis linkage platform (ingot was placed 15 mm below the nozzle). During the experiment, the tank was first filled with the experimental liquid before the pump was turned on, and the liquid flow rate was set using the precision valve and float flowmeter, which allowed liquid flow at a certain flow rate from the nozzle. Simultaneously, the entire process of liquid entering and spreading in the kerf was captured using the high-speed camera.

To clarify the effect of the physical properties of the liquid, three solutions were prepared for the simulations and experimental studies, as shown in Table 2, where μ_l, ρ_l and γ_{lv} are the liquid dynamic viscosity, liquid density, and liquid surface tension, respectively. Solution A is a 2% aqueous solution of a commercially available cutting fluid, solution B is PEG 200 solution, and solution C is deionized water. The prepared solutions represent the cutting fluids commonly used in DWS (mainly water-based coolant) and MWSS (mainly composed of poly-ethylene glycol (PEG)) [10], respectively. All the solutions were prepared and measured at a room temperature of 298.15 K, and the liquid viscosity, surface tension, and density were measured using a digital rotor viscometer (NDJ-8S), liquid surface tension measuring instrument (BZY-B), graduated cylinder, and precision electronic scale, respectively.

2.3 Simulation Parameters

The basic parameters influencing the liquid spreading process typically include the liquid properties, flow velocity, and scale parameters of the flow environment [15]. Therefore, the following simulation parameters were chosen assuming that the liquid density ρ_l= 999.12 is a fixed value in the simulation study: A_k is the area of the kerf center section, D_w is the kerf width, μ_l is the liquid dynamic viscosity, γ_{lv} is the liquid surface tension, and v_i is the liquid velocity at the inlet area of the kerf.

Table 1 Boundary conditions

Zone	Setting
Inlet	Area: 9 mm^2, Velocity-inlet: v_0= 0.1−1.6 m/s
Outlet	Pressure-outlet, gauge pressure: 0
Outer ingot wall	K_s=0.001 mm
Inner kerf wall	K_s=0.005 mm
Kerf surface	K_s=0.030 mm

Table 2 Physical properties of different solutions

Solution	μ_l (mPa·s)	ρ_l (kg/m^3)	γ_{lv}(mN/m)
A	1.53	999.12	49.10
B	31.65	1122.37	45.71
C	0.92	997.31	71.92

where L is a commercially available cutting fluid, solution A is the 2% L aqueous solution, solution B is the PEG 200 solution, solution C is the deionized water. All the solutions are prepared and measured at room temperature of 298.15k

Table 3 Variations of simulation parameters

Parameters	Variations
A_k (mm^2)	223.14, 1013.40, 1782.94, 9120.73, 35342.91
D_w (mm)	0.1, 0.15, 0.2, 0.25, 0.3, 0.4, 0.5
μ_l (mPa·s)	0.92−32.61
γ_{lv} (mN/m)	20−80
v_i (m/s)	0.55, 0.58, 0.67, 0.97, 1.68

The variations in the simulation parameters are shown in Table 3, where A_k and D_w represent the development trend in the industry (ingot diameter D_i= 2, 6, 12 inch) and the actual processing conditions (sawn depth D_s=D_i/5, D_i/2, 4D_i/5), respectively. Additionally, the liquid properties (physical properties of the solutions) were set within a reasonable range (see Table 2). According to Bernoulli's theorem [15, 16], the variations in the v_i are determined using the inlet velocity v_0 (see Table 1) and distance h_i between the inlet and top of the kerf as follows:

$$v_i = \sqrt{v_0^2 + 2gh_i} = \sqrt{v_0^2 + 2 \times 9.8 \times 0.015} = \sqrt{v_0^2 + 0.294}. \tag{1}$$

Moreover, three non-dimensional numbers, Reynolds number $Re = \rho_l v l_0 / \mu_l$, Weber number $We = \rho_l v^2 l_0 / \gamma_{lv}$ and Capillary number $Ca = v\mu_l / \gamma_{lv}$, were introduced to characterize the liquid flow state and analyze simulation results [17]; where v is the fluid flow velocity and l_0 is the characteristic length. For the liquid flow in the kerf, l_0 is equal to the kerf width D_w, similar to the flow between parallel plates [18]. In this study, the maximum Reynolds number Re_{max} in the kerf can be approximately obtained as:

$$Re_{max} \approx \frac{\rho_{l\,max} v_{i\,max} l_{0\,max}}{\mu_{l\,min}} = \frac{1122.37 \times 1.68 \times 0.0005}{0.00092} \approx 1024.7. \tag{2}$$

Since Re_{max} is less than the lower bound of the critical Reynolds number Re_c (2000) [18], the liquid in the kerf is laminar. For a $Re \gg 1$, the quantity of interest in the effect of the surface tension is determined using the Weber number [19], and the minimum weber number is approximated as follows:

$$We_{min} \approx \frac{\rho_{l\,min} v_{i\,min}^2 l_{0\,min}}{\gamma_{lv\,min}}$$
$$= \frac{999.12 \times 0.55^2 \times 0.0001}{0.08} = 0.37. \tag{3}$$

Hence, the effect of the surface tension should not be neglected since the Weber number $We<1$ [18].

2.4 Governing Equations and Solving Method

Since two-phase flow is involved in this study, a volume of fluid (VOF) method was introduced to capture the gas-liquid interface. In the VOF model, the volume fraction of each fluid is tracked down through each cell in the domain [20]. For the fluid i, the volume fraction α_i is defined as follows:

$\alpha_i = 0$: The cell has no fluid i.

$\alpha_i = 1$: The cell is full of the fluid i.

$\alpha_i < 0$: The cell has an interface between the fluid i and one or more other fluids.

Subsequently, the continuity equation for the volume fraction was solved to track the interface. Assuming that the subscript i represents the fluid i, the continuity equation has the following form [21]:

$$\frac{\partial \alpha_i}{\partial t} + \nabla \cdot (\alpha_i \vec{v}_i) = 0. \tag{4}$$

Moreover, the fluid properties in the continuity equation are determined based on their phase components in each control volume. For the two-phase flow in this study, the density and viscosity are given by:

$$\rho = \alpha_j \rho_j + \alpha_i \rho_i, \tag{5}$$

$$\mu = \alpha_j \mu_j + \alpha_i \mu_i, \tag{6}$$

where the subscript j represents fluid j. Depending on the fluid properties, a momentum equation is then solved for the velocity field that is shared among the phases [21]:

$$\frac{\partial}{\partial t}(\rho \vec{v}) + \nabla \cdot (\rho \vec{v} \vec{v}) = -\nabla p + \nabla \cdot \left[\mu \left(\nabla \vec{v} + \nabla \vec{v}^{\mathrm{T}} \right) \right] + \rho \vec{g} + \vec{F}, \tag{7}$$

where p is the static pressure, $\rho \vec{g}$ is the gravitational body force and $\vec{F}$ is the external body force defined using the source terms.

Considering the significance of the surface tension, a continuum surface force (CSF) model [22] was introduced. Here, the surface tension can be expressed according to the volume force F_v across the spreading interface, which was added to the VOF model through the source terms of the momentum equation, and can be given as follows [23]:

$$F_v = \gamma_{ij} \frac{2\rho k \nabla \alpha_i}{\left(\rho_i + \rho_j \right)}, \tag{8}$$

where γ_{ij} is the surface tension between the two phases, $n = \nabla \alpha_i$ is the surface normal, $k = \nabla \cdot \hat{n}$ is the surface curvature, and $\hat{n} = n/|n|$ is the unit normal vector to the interface. Moreover, a wall adhesion term is introduced to specify $\hat{n}$ at the liquid-solid-gas interface [24]:

$$\hat{n} = \hat{n}_w \sin \theta_d + \hat{t}_w \cos \theta_d, \tag{9}$$

where $\hat{n}_w$ and $\hat{t}_w$ are the unit vectors normal and tangential to the solid wall, and θ_d is the dynamic contact angle between the liquid and wall. Based on Hoffman's systematic study [25] of the θ_d in glass capillary tubes, Jiang et al. [26] deduced an empirical correlation which fits the data equally well:

$$\frac{\cos \theta_d - \cos \theta_s}{\cos \theta + 1} = -\tanh \left(4.96 Ca^{0.702} \right), \tag{10}$$

where θ_s is the static contact angle between liquid and wall. In this paper, the free liquid jet flows from the top to the kerf; hence, θ_s is assumed to be similar to the initial contact angle θ_0 when the liquid just reaches the kerf. As shown in Figure 4, θ_0 can be defined as: $\theta_0 \approx 90° + \arcsin(D_w/D_l)$. Additionally, because D_w is much smaller than the diameter of the liquid jet

$D_l = 0.004$, $\theta_s \approx \theta_0 \approx 90°$. Eq. (10) was then reduced to Eq. (11) to characterize the dynamic contact angle:

$$\cos \theta_d = -\tanh \left(4.96 Ca^{0.702} \right). \tag{11}$$

The computational model was then implemented into the Ansys Fluent software for calculation. Here, the momentum equations were solved using the pressure-based solver, and the continuity equation was solved via implicit time discretization. For pressure velocity coupling, the pressure implicit splitting of operators (PISO) scheme [27] was used, and to calculate the calculation accuracy, the global Courant number was set to 0.2 using an adaptive time step. In addition, a dynamic contact angle was introduced using user defined functions (UDF).

The following assumptions were made before the simulation setup: (1) both the air and liquid are incompressible fluids, (2) the motion of the wire is not considered and the surface of the kerf is a stationary plane, (3) heat transfer is not taken into account because the focus of this study is the liquid flow regimes in the sawn kerf, and the entire process is thermostatic at a temperature of 298.15 K.

3 Results

3.1 Liquid Entering-Spreading Progress

A simulation research was first conducted under the following parameters, which are close to the general situation: D_i= 50.8 mm, A_k=1013.4 mm², D_w= 0.3 mm, v_i= 0.4 m/s, and the liquid properties of the solution A.

The 3D liquid flow state outside the kerf is shown in Figure 5(a). From Figure 5(a)i, the liquid first flows from the top to bottom before coming into contact with the
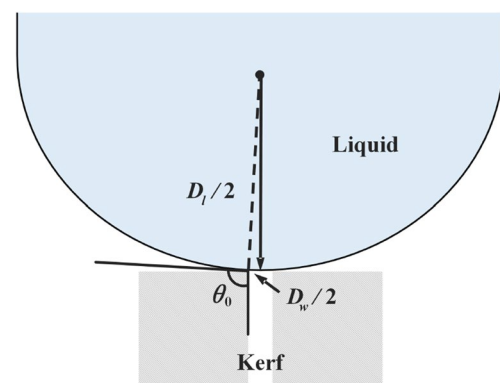
Figure 4 Schematic of the initial contact angle when the liquid just reaches the kerf

ingot, and a liquid layer is then gradually formed at the outer edge of the kerf (Figure 5(a)iii−vi). Moreover, the evolution of the liquid contour in the center section of the kerf is shown in Figure 5(b). As the liquid reaches the upper surface of the ingot (Figure 5(b)i), it enters the kerf (Figure 5(b)ii) and spreads downward with an arc-shaped gas-liquid interface (Figure 5(b)iii). Subsequently, the spreading liquid reaches the kerf surface and gradually covers the sawing area (Figure 5(b)iv). Finally, it saturates the kerf and maintains an equilibrium state (Figure 5(b)v and vi) when $T \geq 0.45$ s.

To evaluate the spreading behavior, the liquid flow time to reach the equilibrium state t_e is taken as an evaluation index in the following section.

3.2 Parametric Simulation
3.2.1 Effect of Kerf Area
Figure 6 shows the simulation results of various A_k (simulation parameters: A_{k1}= 223.14 mm^2, T= [0.07, 0.11, 0.21] s; A_{k2}= 1013.4 mm^2, T= [0.27, 0.35, 0.45] s; A_{k3}= 1782.94 mm^2, T= [0.49, 0.58, 0.74] s; A_{k4}= 9120.73 mm^2, T= [1.92, 5.95] s; A_{k5}= 35342.91 mm^2; T= [2.71, 17.80] s; other simulation parameters: D_w= 0.3 mm, v_i= 0.67 m/s, liquid properties of the solution A). The evolution of the liquid contours is presented using a scatter plot of t_e. It should be noted that the liquid spreading interface gradually transforms from arc-shape to a U-shape with an increase in the A_k. However, there is no fundamental discrepancy in the liquid spreading regimes: the liquid that flows into the kerf from the top to bottom spreads to both sides after reaching the center of the sawing area before finally reaching an equilibrium state. Moreover, the results of A_{k4} and A_{k5} show that the kerf cannot be filled
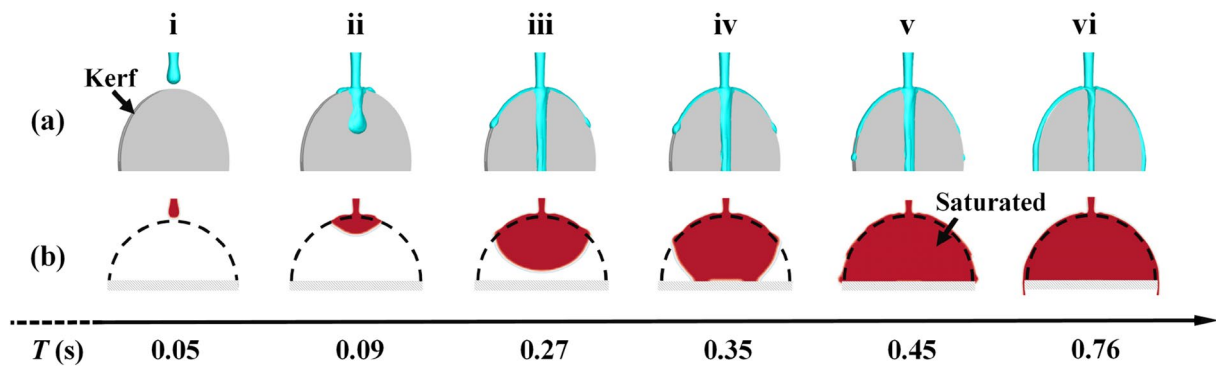

Figure 5 Liquid entering-spreading process in the kerf: (**a**) 3D plot of the liquid dynamic flow state, (**b**) Transient evolution of the liquid contours in the center section of the kerf
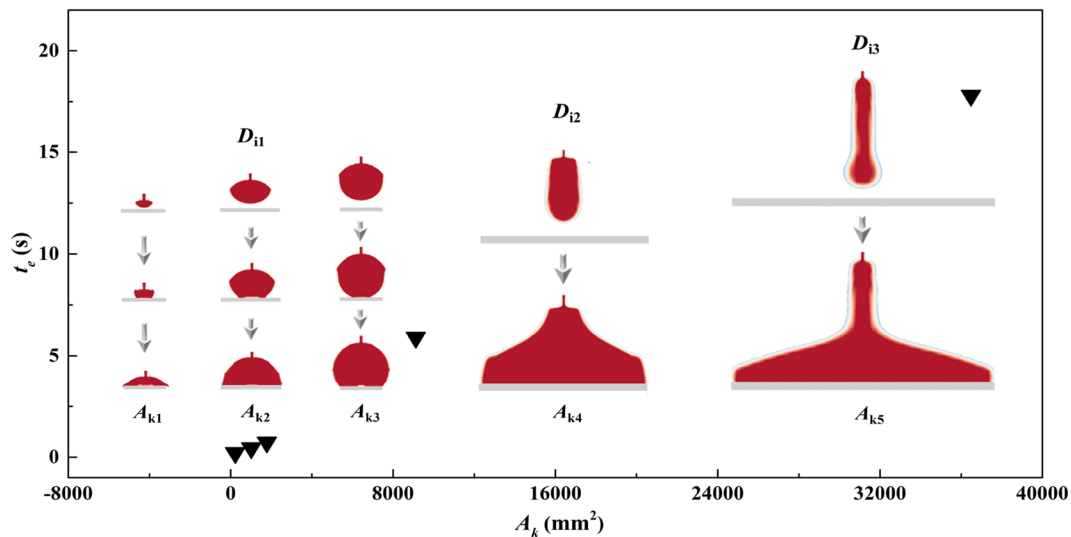

Figure 6 Plot of the liquid flow time to reach the equilibrium in different kerf areas, and the evolution of the liquid spreading contour

after the liquid contour is stable (Figure 6), which is attributed to the insufficient liquid flow. Further, t_e significantly increases with increasing A_k (Figure 6), which also indicates that a higher liquid flow is required for a larger A_k.

3.2.2 Effect of Kerf Width

The simulation results of various D_w are shown in Figure 7 (simulation parameters: D_{w1}= 0.5 mm, T= [0.14, 0.35] s; D_{w2}= 0.4 mm, T= [0.20, 0.39] s; D_{w3}= 0.3 mm, T= [0.30, 0.45] s; D_{w4}= 0.2 mm, T= [0.45, 1.04] s; D_{w5}= 0.1 mm, T= [0.35, 4.08] s; A_{k2}= 1013.4 mm^2, v_i= 0.67 m/s, liquid properties of solution A). t_e exhibits an increasing trend as D_w declines, and significantly increases when D_w> D_{w4}. Typically, a decrease in D_w makes it more difficult for the liquid to spread in the kerf. Meanwhile, the spreading contours show a clear discrepancy in the cases of various D_w. In cases D_{w1}, D_{w2} and D_{w3}, the liquid spreads with arc-shaped gas-liquid interfaces with different curvatures. However, in cases D_{w4} and D_{w5}, distinct air chambers are noted in the kerf.

The formation process of the air chamber phenomenon is shown in Figure 8 (simulation parameters: D_i= 50.8 mm, A_k=1013.4 mm^2, D_w= 0.1 mm, v_i= 0.4 m/s, liquid properties of solution A). It can be observed that for case D_{w5}, the liquid spreads to both sides when it enters the kerf (Figure 8i). Subsequently, the incoming liquid slides along the outer edge of the kerf (Figure 8ii). A small amount of the liquid then gradually seeps into the kerf (Figure 8(b)iii) and wraps it in a liquid layer, forming an air chamber in the kerf. Furthermore, as the liquid slowly spreads and squeezes downward, an opening is created in the wrapped liquid layer (Figure 8iv), from which air is squeezed out. Therefore, the liquid spreads to the kerf surface and gradually expels the air (Figure 8(b)v) before finally reaching an equilibrium state (Figure 8(b)vi).
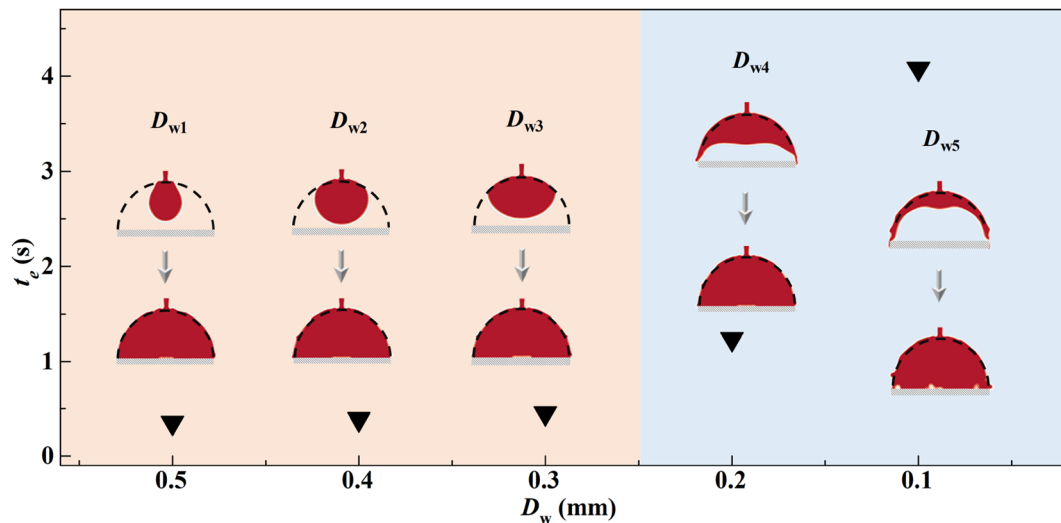

Figure 7 Plot of the liquid flow time to reach an equilibrium for different kerf widths, and the evolution of the liquid spreading contour
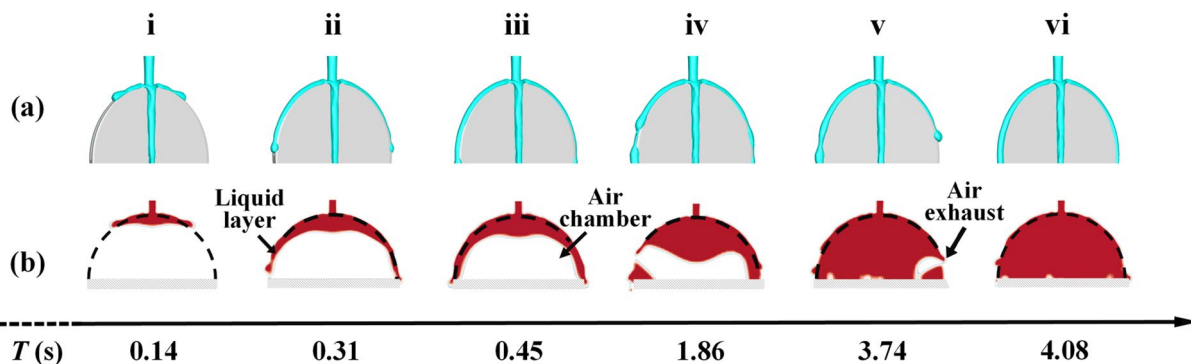

Figure 8 Results of the simulations under a kerf width of 0.1 mm: (**a**) 3D plot of the liquid dynamic flow regime, (**b**) Transient evolution of the liquid contours in the center section of the kerf

3.2.3 Effect of Liquid Viscosity

The simulation results for the various liquid viscosities μ_l, and the liquid spreading contours at a liquid flow time of 0.3 s are presented in Figure 9, (simulation parameters: D_i= 50.8 mm, A_k= 1013.4 mm², D_w= 0.3 mm, v_i= 0.67 m/s, γ_{lv}= 50 mN/m, ρ_l= 999.12), where t_e shows an accelerated increasing trend with μ_l, based on the plotted liquid spreading contours. Moreover, a sharp increase in t_e is seen between μ_{l2} and μ_{l3} (as indicated by the red arrow). This could be attributed to the formation of the air chamber phenomenon when $\mu_l \geq \mu_{l3}$ (see Figure 9). By comparing the liquid spreading area using the same flow time (0.3 s), it was confirmed that the grow of μ_l significantly reduces the liquid spreading rate in the kerf and contributes to the air chamber phenomenon.

3.2.4 Effect of Liquid Surface Tension

The simulation results for the various liquid surface tensions γ_{lv}, and the liquid spreading contours at a liquid flow time of 0.3 s are presented in Figure 10 (simulation parameters: D_i= 50.8 mm, A_k= 1013.4 mm², D_w= 0.3 mm, v_i= 0.67 m/s, μ_l= 3 mPa·s, ρ_l= 999.12 kg/m³). The profile of t_e shows an upward trend as γ_{lv} increases, and a growth spurt is presented between γ_{lv3} and γ_{lv4}. Moreover, as γ_{lv} increases, the spreading interface gradually evolves from an arc-shape (γ_{lv1}) to a flatter shape (γ_{lv2} and γ_{lv3}), further forming a liquid layer that wraps the kerf and inducing the occurrence of the air chamber phenomenon in the kerf ($\gamma_{lv} \geq \gamma_{lv4}$). Therefore, it is speculated that the different spreading regimes can be mutually-transform when the parameters are altered within a certain limit. Therefore, it can be concluded that
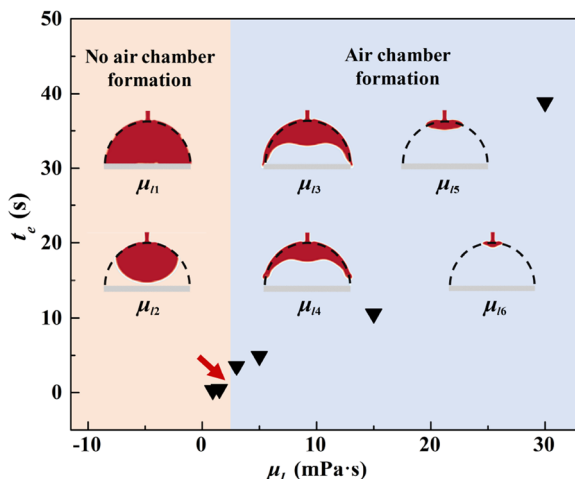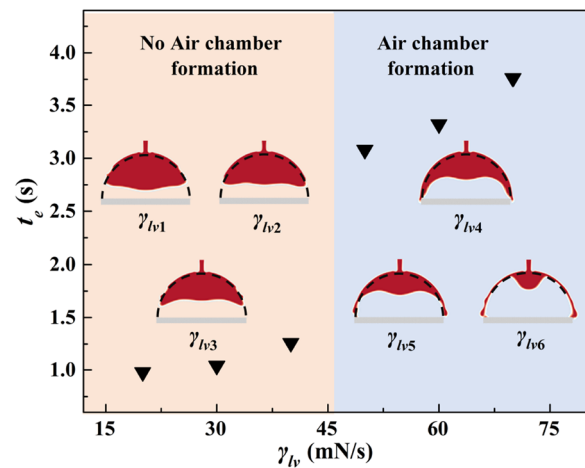
Figure 10 Plot of the time required to the reach the equilibrium state under various liquid surface tensions: γ_{lv1}= 20 mN/m, γ_{lv2}= 30 mN/m, γ_{lv3}= 40 mN/m, γ_{lv4}= 50 mN/m, = 60 mN/m, γ_{lv5}= 70 mN/m

the reduction in γ_{lv} facilitates liquid spreading in the kerf and assists in avoiding the formation of an air chamber.

3.2.5 Effect of the Liquid Inlet Velocity

Figure 11 presents the simulation results for various liquid velocities v_i, and the liquid spreading contours at a liquid flow time of 0.4 s (simulation parameters: D_i= 50.8 mm, A_k= 1013.4 mm², D_w= 0.2 mm, μ_l= 3 mPa·s, γ_{lv}= 80 mN/m, ρ_l= 999.12 kg/m³). For the plotted liquid spreading contours, t_e shows an accelerated increasing trend as v_i decreases. Moreover, a special phenomenon is observed when $v_i = v_{i3}$, where almost no liquid could flow into the kerf, and t_e is considered to be infinite. Furthermore, as v_i decreases, the evolution of the spreading

Figure 9 Plot of the liquid flow time to the equilibrium for various liquid dynamic viscosities: μ_{l1}= 1 mPa·s, μ_{l2}= 1.5 mPa·s, μ_{l3}= 3 mPa·s, μ_{l4}= 5 mPa·s, μ_{l5}= 15 mPa·s, μ_{l6}= 30 mPa·s
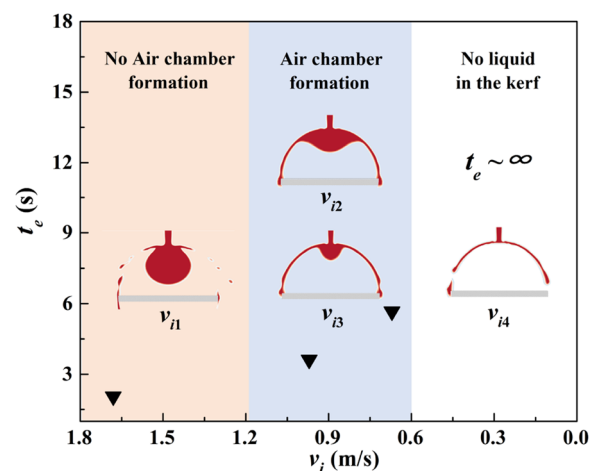
Figure 11 Plot of the time required to reach the equilibrium state for various liquid velocities at the inlet area of the kerf: v_{i1}=1.68 m/s, v_{i2}= 0.97 m/s, v_{i3}= 0.67 m/s, v_{i4}= 0.55 m/s

interface is observed again, where the spreading interface gradually evolves from an arc-shape (v_{i1}) to a liquid layer wrapping the kerf (v_{i2} and v_{i3}). Eventually, the liquid could barely enter the kerf (v_{i4}).

4 Discussion

In the preceding section, numerical simulations were conducted to obtain the liquid spreading regime in the kerfs. By comparing the transient evolution of the liquid spreading contour, three typical liquid spreading regimes were found: (I) The liquid spreads in an up-down direction with an arc-shaped interface; (II) the spreading liquid wraps the outer contour of the kerf, forming an air chamber in the kerf; and (III) the liquid can barely enter the kerf.

4.1 Experimental Verification

Experimental verifications were conducted focusing on the three liquid spreading regimes. Here, the experimental parameters are basically the same as those of the simulations. As shown in Figure 12(a), (b), the simulation and experimental results of solution A have very similar evolutions of the liquid spreading contour with corresponding flow times, which comprise arc-shaped spreading interfaces. This confirms the existence of liquid spreading regime I.

As shown in Figure 13(a), (b), similar liquid spreading evolution process can be observed, and the air chamber phenomenon is seen in both the simulation and experimental results of solution B. This confirms the existence of regime II.

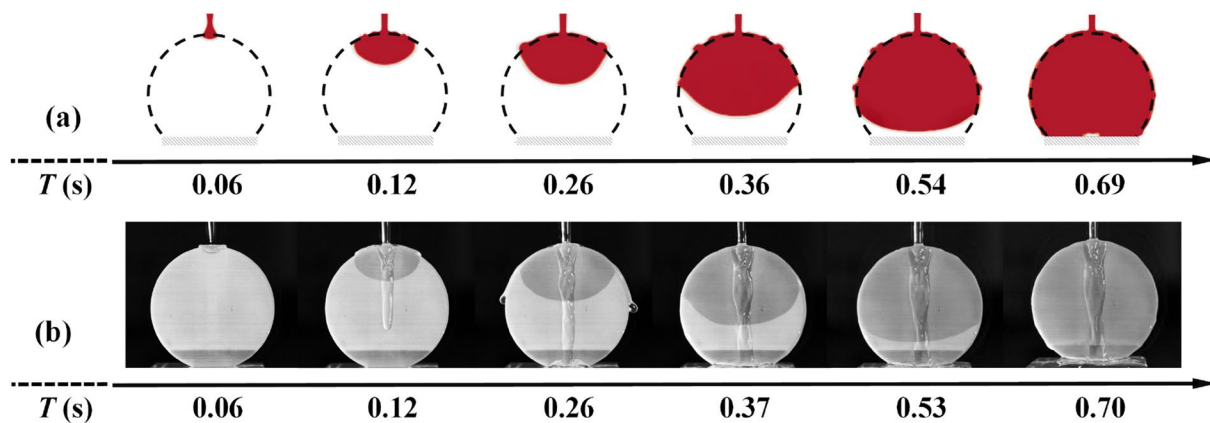As shown in Figure 14(a)–(c), a very similar evolution of the liquid spreading contour is observed in both the

Figure 12 Transient evolution of the spreading contours of solution A in the kerf: (**a**) Simulation results (A_k= 1782.94 mm^2, D_i=50.8 mm, D_w= 0.25 mm, v_i= 0.67 m/s), (**b**) Experimental results ($A_k \approx$ 1780.14 mm^2, D_i=50.8 mm, D_w= 0.253 mm, v_i= 0.41 m/s)
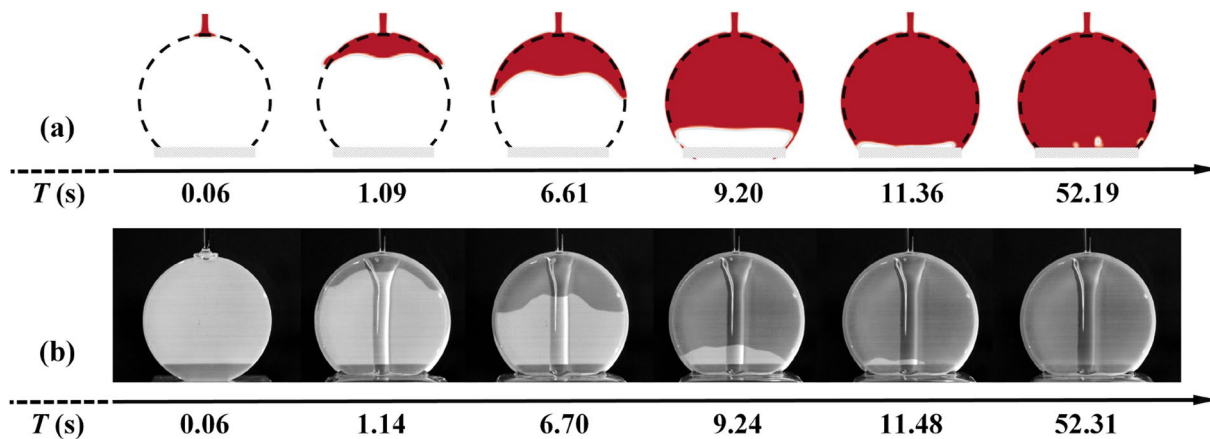

Figure 13 Transient evolution of the spreading contours of solution B in the kerf: (**a**) Simulation results (A_k= 1782.94 mm^2, D_i=50.8 mm, D_w= 0.25 m, v_i= 0.67 m/s), (**b**) Experimental results ($A_k \approx$ 1780.14 mm^2, D_i=50.8 mm, D_w= 0.253 mm, v_i= 0.403 m/s)

simulation and experimental results, where the liquid barely enters the kerf and just spreads around the outer edge. This proves the existence of liquid spreading regime III.

4.2 Causes and Influences of Spreading Regimes

To determine the causes of different spreading regimes, typical simulation cases are selected, and the liquid contours, velocity vector, and pressure in the kerf for a certain flow time are shown in Figure 15 (simulation parameters: (I) $D_i = 50.8$ mm, $A_k = 1013.4$ mm^2, $D_w = 0.3$ mm, $v_i = 0.67$ m/s, liquid properties of solution A, $T = 0.3$ s; (II) $D_i = 50.8$ mm, $A_k = 1013.4$ mm^2, $D_w = 0.1$ mm, $v_i = 0.67$ m/s, liquid properties of solution A, $T = 0.45$ s; (III) $D_i = 50.8$ mm, $A_k = 1013.4$ mm^2, $D_w = 0.2$ mm, $v_i = 0.58$ m/s, $\mu_l = 3$ mPa·s, $\gamma_{lv} = 80$ mN/m, $\rho_l = 999.12$ kg/m^3, $T = 0.3$ s).

For spreading regime I, a significant pressure gradient (approximately 230−0 Pa, see Figure 15(b)-I) is observed between the kerf top and spreading interface, which can cause a large spreading velocity in the kerf [28, 29]. This is attributed to the significant velocity vector in the kerf, both in the liquid and air phases (Figure 15(a)-I). Thus, the liquid can spread with an arc-shaped interface in the kerf.

For spreading regime II, there is a high pressure gradient at the outer edge of the kerf (about 230−30 Pa,
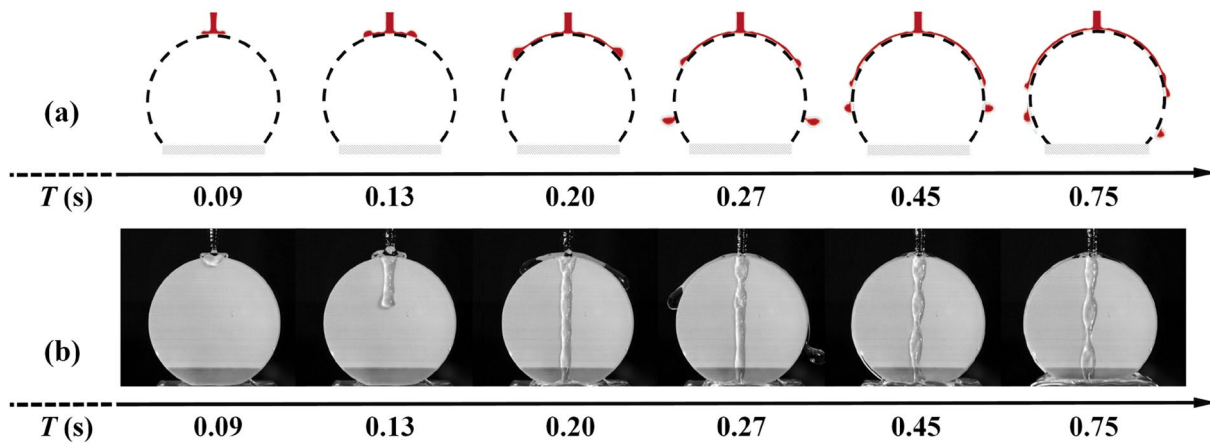
Figure 14 Transient evolution of the spreading contours of solution C in the kerf: (**a**) Simulation results ($A_k = 1782.94$ mm^2, $D_i = 50.8$ mm, $D_w = 0.25$ m, $v_i = 0.55$ m/s), (**b**) Experimental results ($A_k \approx 1780.14$ mm^2, $D_i = 50.8$ mm, $D_w = 0.253$ mm, $v_i = 0.55$ m/s)
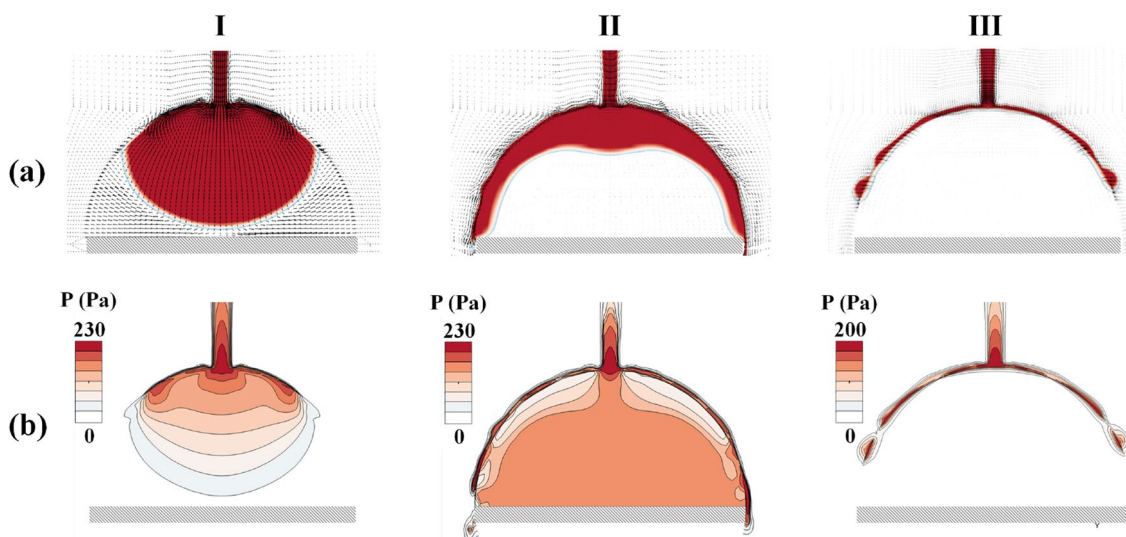

Figure 15 Three typical spreading regimes and their corresponding (**a**) vector diagrams and (**b**) total pressure nephograms

Figure 15(b)-II) where the velocity vector is significant. However, the pressure gradient is between the kerf top and the spreading interface is very small (approximately 230−170 Pa, see Figure 15(b)-II), making the velocity vector almost invisible. Hence, the liquid is more likely to seep in from the outer edge and form a liquid layer that wraps the kerf, which results in the generation of an air chamber.

For spreading regime III, there are no liquid pressure gradients and velocity vectors in the kerf; consequently, the liquid barely enters the kerf.

Overall, in spreading regime I, the liquid spreads easier and quicker in the kerf to expel air from the sawing area, infiltrate the processing area, and achieve its important functions. However, in spreading regime II, the air chamber significantly hinders the spreading behavior of the liquid and increases the probability of dry cutting during sawing. In spreading regime III, dry cutting has a high likeliness of occurring [30], especially for MWSS, causing the abrasive to not be carried by the liquid to the sawing area. Therefore, it is very detrimental to wire sawing.

4.3 Non-Dimensional Analysis

These results show that a decrease in the A_k, μ_l, γ_{lv}, and the growth of the D_w and v_i result in a reduction in the t_e, which means that the liquid spreads better in the kerf. However, in-depth analysis is yet to be conducted on the interplay of these parameters and their synergy effects on the spreading behavior. Moreover, it can be seen from Figures 10, 11 that the different spreading regimes can be mutually transformed when the parameters are altered to a certain extent. To determine the mechanism, extensive numerical simulations were conducted (all relevant simulation parameters and results are shown in Table 6, see Appendix) owing to their significant influence on small-scale liquid flow.

Meanwhile, non-dimensional analysis was performed to explore the synergy effect of the parameters using two typical dimensionless numbers, the Weber number and Capillary number, which were used owing to their significant influence on small-scale liquid flow [19, 30]. The Weber and Capillary numbers were each used to represent different simulation cases: $We_r = \rho_l v_i^2 l_0 / \gamma_{lv}$ and Ca_r, and the simulations were carried out within certain limits of the We_r (5−300) and Ca_r (0.3−8).

The comprehensive simulation results for the non-dimensional parameters We_r and Ca_r are plotted in Figure 16. The log-log plot shows that there are clear boundaries between the three spreading regimes. This explains the mechanism of the mutual transformation between spreading regimes. Moreover, the two boundary lines were written by fitting the data in the boundary area using (both with $R^2 \approx 0.99$):

$$l_1: We_r = 24.8 Ca_r^{0.65}, \tag{12}$$

$$l_2: We_r = 1.47 Ca_r^{0.1}. \tag{13}$$

Therefore, a predictive model is proposed for identifying the liquid spreading regime, which is given using a set of Webb and Capillary numbers:

$$\begin{cases} \text{Regime I}: We_r > 24.8 Ca_r^{0.65}, \\ \text{Regime II}: 1.47 Ca_r^{0.1} < We_r < 24.8 Ca_r^{0.65}, \\ \text{Regime III}: We_r < 1.47 Ca_r^{0.1}. \end{cases} \tag{14}$$

Before the actual processing, the Weber ($Ca_r = \mu_l v_i / \gamma_{lv}$) and Capillary numbers ($We_r = \rho_l v_i^2 l_0 / \gamma_{lv}$) were calculated by measuring parameters such as the kerf width D_w ($l_0 \approx D_w$), the liquid flow rate v_i, the liquid density ρ_l, the viscosity μ_l, and the surface tension γ_{lv}. For a given set of Weber and Capillary numbers, the liquid spreading regime can be predicted as: When $We_r > 24.8 Ca_r^{0.65}$,
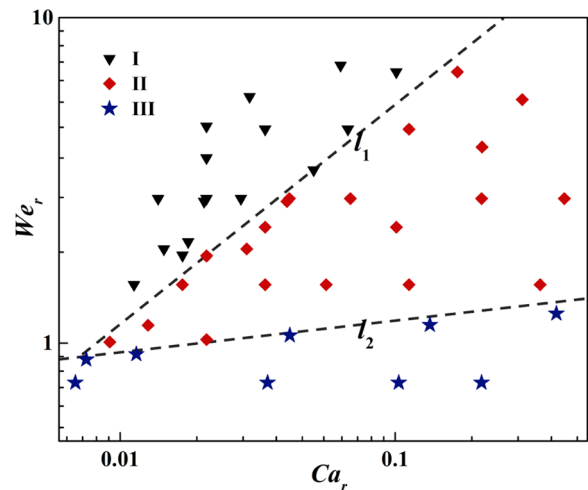

Figure 16 Non-dimensional map of the simulation results

the liquid spreads according to regime I; when $1.47Ca_r^{0.1} < We_r < 24.8Ca_r^{0.65}$, the liquid spreads according to regime II; and when $We_r < 1.47Ca_r^{0.1}$, the liquid spreads according to regime III.

This paper provides insight into the influence of the liquid spreading behavior in kerfs during wire sawing. It also provides a new approach for solving problems that may be encountered during wire sawing. However, additional studies should be conducted to corroborate the application of the dynamic contact angle model in 3D geometry. Furthermore, the high validity simulation method used in this paper may contribute to the research on the filling flow in small scales, such as fluid problems in precision machining, and micro injection molding.

5 Conclusions

(1) This study was designed to investigate the liquid spreading behavior in wire-sawn kerfs. A CFD simulation model was established, and parametric simulations were successfully conducted to identify the effect of the kerf area, kerf width, liquid viscosity, liquid surface tension, and liquid velocity at the inlet of the kerf.

(2) Based on the development trend in wire sawing, an increase in the wafer area does not change the liquid spreading regime in the kerf, but a reduction in the kerf width significantly hinders the liquid spreading behavior. By adjusting the physical properties and supply conditions of the liquid, the spreading regime can be effectively converted to facilitate wire sawing.

(3) Three typical liquid spreading regimes were found in both the simulation and experimental results: (I) The liquid spreads in the up-down direction with an arc-shaped interface; (II) the spreading liquid wraps the outer contour of the kerf and forms an air chamber in the kerf; and (III) the liquid barely enters the kerf. Moreover, the limiting conditions of the three spreading regimes are identified using a non-dimensional analysis, and a prediction model

for the liquid spreading regime is proposed using a given set of Weber and Capillary numbers. When $We_r > 24.8Ca_r^{0.65}$, the liquid spreads according to regime I; when $1.47Ca_r^{0.1} < We_r < 24.8Ca_r^{0.65}$, the liquid spreads according to regime II; and when $We_r < 1.47Ca_r^{0.1}$, the liquid spreads according to regime III.

Appendix
See Tables 4, 5, 6

Table 4 Parameters of the geometric model

D_i (mm)	A_k (mm)	D_w (mm)
50.8	223.14	0.3
	1013.4	0.1, 0.2, 0.25, 0.3, 0.4, 0.5
	1782.94	0.3
152.4	9120.73	0.3
304.8	35342.91	0.3

Table 5 Wire sawing conditions and parameters

Sawing conditions and parameters	
Machine model	**JXQ-1201**
Sawing method	Single wire sawing
Wire speed	6 m/s
Table speed	0.15 mm/min
Wire tension	25 N
Sawing interval	50 m−1050 m
Ingot diameter	2-inch ingot with a length of 50 mm
Diamond wire saw	Wire diameter 0.18 mm, diamond particle size 30 μm−40 μm
Sawn depth	42.381 mm
Sawn width	0.223 mm

Table 6 Simulation parameters and results in the non-dimensional analysis (*R* refers to the spreading regimes in the kerf)

D_w (m)	μ_l (N/m·s)	γ_{lv} (N/m)	v_i (m/s)	ρ_l (kg/m³)	We_r	Ca_r	R
0.0001	0.0015	0.049	0.67	999.12	0.925	0.021	II
0.0002	0.0015	0.049	0.67	999.12	1.851	0.021	II
0.0003	0.0015	0.049	0.67	999.12	2.777	0.021	I
0.0004	0.0015	0.049	0.67	999.12	3.702	0.021	I
0.0005	0.0015	0.049	0.67	999.12	4.628	0.021	I
0.0003	0.0300	0.049	0.67	999.12	2.777	0.413	II
0.0003	0.0150	0.049	0.67	999.12	2.777	0.206	II
0.0003	0.0050	0.049	0.67	999.12	2.777	0.069	II
0.0003	0.0030	0.049	0.67	999.12	2.777	0.041	II
0.0003	0.0020	0.049	0.67	999.12	2.777	0.028	I
0.0003	0.0015	0.049	0.67	999.12	2.777	0.021	I
0.0003	0.0010	0.049	0.67	999.12	2.777	0.014	I
0.0003	0.0015	0.030	0.67	999.12	4.536	0.034	I
0.0003	0.0015	0.050	0.67	999.12	2.722	0.020	I
0.0003	0.0015	0.070	0.67	999.12	1.944	0.014	I
0.0003	0.0015	0.080	0.67	999.12	1.701	0.008	I
0.0003	0.0015	0.080	0.55	999.12	1.139	0.007	I
0.0003	0.0015	0.049	0.55	999.12	1.860	0.017	I
0.0003	0.0015	0.049	0.58	999.12	2.043	0.018	I
0.0003	0.0015	0.049	0.67	999.12	2.777	0.021	I
0.0003	0.0015	0.049	0.96	999.12	5.713	0.030	I
0.0003	0.0015	0.049	1.68	999.12	17.45	0.052	I
0.0002	0.0100	0.060	0.67	999.12	1.512	0.112	II
0.0002	0.0050	0.060	0.67	999.12	1.512	0.056	II
0.0002	0.0030	0.060	0.67	999.12	1.512	0.034	II
0.0002	0.0015	0.060	0.67	999.12	1.512	0.017	II
0.0002	0.0010	0.060	0.67	999.12	1.512	0.011	I
0.0003	0.0150	0.070	0.96	999.12	3.999	0.207	II
0.0003	0.0150	0.060	0.96	999.12	5.599	0.290	II
0.0003	0.0050	0.020	0.67	999.12	6.804	0.168	II
0.0003	0.0050	0.030	0.67	999.12	4.536	0.112	II
0.0003	0.0015	0.020	0.67	999.12	6.804	0.101	I
0.0003	0.0015	0.030	0.67	999.12	4.536	0.067	I
0.0003	0.0015	0.040	0.67	999.12	3.402	0.051	I
0.0003	0.0015	0.050	0.67	999.12	2.722	0.040	II
0.0003	0.0015	0.060	0.67	999.12	2.268	0.034	II
0.0003	0.0015	0.070	0.67	999.12	1.944	0.029	II
0.0002	0.0010	0.072	0.55	999.12	0.898	0.007	III
0.0002	0.0015	0.072	0.55	999.12	0.923	0.011	III
0.0002	0.0050	0.070	0.58	999.12	1.056	0.041	III
0.0002	0.0150	0.065	0.58	999.12	1.137	0.133	III
0.0002	0.0400	0.060	0.58	999.12	1.2328	0.386	III
0.0002	0.0010	0.08	0.55	999.12	0.755	0.006	III
0.0002	0.0050	0.08	0.55	999.12	0.755	0.034	III
0.0002	0.0150	0.08	0.55	999.12	0.755	0.103	III
0.0002	0.0300	0.08	0.55	999.12	0.755	0.206	III

Authors' information

Lin Lin, born in 1993, is currently a doctor candidate at *Xiamen University, China*. He received his master degree from *Huaqiao University, China*, in 2020. His research focus on micro/nano robots' mechanical effects and their associated biomedical applications.

Hui Huang, born in 1974, is currently a professor at *Huaqiao University, China*. He received his Ph.D degree in 2002 from *Nanjing University of Aeronautics and Astronautics, China*. His research interests include the machining of brittle material and manufacturing of superabrasive tools.

Availability of Data and Materials

The datasets supporting the conclusions of this article are included within the article.

Declarations

Ethics Approval and Consent to Participate

Not applicable.

Consent for Publication

Not applicable.

Competing Interests

The authors declare no competing financial interests.

References

[1] H J Möller. Basic mechanisms and models of multi-wire sawing. *Advanced Engineering Materials*, 2004, 6(7): 501-513.

[2] Rakshit, Rahul, Alok Kumar Das. A review on cutting of industrial ceramic materials. *Precision Engineering*, 2019, 59: 90-109.

[3] H Wu. Wire sawing technology: A state-of-the-art review. *Precision Engineering*, 2016, 43: 1-9.

[4] F Wallburg, M Kuna, M Budnitzki, et al. A material removal coefficient for diamond wire sawing of silicon. *Wear*, 2022, 504: 204400.

[5] Y Gao, P Ge, L Z hang, et al. Material removal and surface generation mechanisms in diamond wire sawing of silicon crystal. *Materials Science in Semiconductor Processing*, 2019, 103: 104642.

[6] M Shinya, T Yazawa, T Otubo. Study on the slicing of sapphire using a wire tool. *Advanced Materials Research*, 2015, 1136: 333-337.

[7] X Huang, H Huang, H Guo. Simulation and experimental research on the slicing temperature of the sapphire with diamond wire. *International Journal of Computational Methods*, 2019, 16(4): 1843003.

[8] M Bhagavat, V Prasad, I Kao. Elasto-hydrodynamic interaction in the free abrasive wafer slicing using a wiresaw: modeling and finite element analysis. *Journal of Tribology*, 2000, 122(2): 394-404.

[9] F Yang, I Kao. Free abrasive machining in slicing brittle materials with wire saw. *Journal of Electronic Packaging*, 2001, 123(3): 254-259.

[10] S Bhagavat, I Kao. A finite element analysis of temperature variation in silicon wafers during wiresaw slicing. *International Journal of Machine Tools and Manufacture*, 2008, 48(1): 95-106.

[11] L Johnsen, J E Olsen, T Bergstrom, et al. Heat transfer during multiwire sawing of silicon wafers. *Journal of Thermal Science and Engineering Applications*, 2012, 4(3): 31006-31013.

[12] D Lindholm, D Mortensen, H Fjær, et al. A computer model and methodology to predict temperatures and deformations during diamond multi-wire cutting. *AIP Conference Proceedings. AIP Publishing LLC*, 2018, 1999(1): 140002.

[13] K I Ishikawa, H Suwabe, S Itoh, et al. A basic study of the behavior of slurry action at multi-wire saw. *Key Engineering Materials*, 2003, 238: 89-92.

[14] B Nassauer, A Hess, M Kuna. Numerical and experimental investigations of micromechanical processes during wire sawing. *International Journal of Solids & Structures*, 2014, 51(14): 2656-2665.

[15] B E Faulkner, F M Ytreberg. Understanding Bernoulli's principle through simulations. *American Journal of Physics*, 2011, 79(2): 214-216.

[16] A W Glaspell, V J Rouse, B K Friedrich, et al. Heat transfer and hydrodynamics of air assisted free water jet impingement at low nozzle-to-surface distances. *International Journal of Heat and Mass Transfer*, 2019, 132: 138-142.

[17] B K Primkulov, A A Pahlavan, X Fu, et al. Signatures of fluid–fluid displacement in porous media: Wettability, patterns and pressures. *Journal of Fluid Mechanics*, 2019, 875: R4.

[18] J H Ferziger, M Peric, A Leonard. Computational methods for fluid dynamics. *Physics Today*, 1997, 50(3): 80-84.

[19] J W J Kaiser, J M Winter, S Adami, et al. Investigation of interface deformation dynamics during high-Weber number cylindrical droplet breakup. *International Journal of Multiphase Flow*, 2020, 132: 103409.

[20] Issakhov, Alibek, Medina Imanberdiyeva. Numerical simulation of the movement of water surface of dam break flow by VOF methods for various obstacles. *International Journal of Heat and Mass Transfer*, 2019, 136: 1030-1051.

[21] S V Ershkov, E Y Prosviryakov, N V Burmasheva, et al. Towards understanding the algorithms for solving the Navier–Stokes equations. *Fluid Dynamics Research*, 2021, 53(4): 044501.

[22] H S H Mohand, H Hoang, G Galliero, et al. On the use of a friction model in a Volume of Fluid solver for the simulation of dynamic contact lines. *Journal of Computational Physics*, 2019, 393: 29-45.

[23] C W Hirt, B D Nichols. Volume of fluid (VOF) method for the dynamics of free boundaries. *Journal of Computational Physics*, 1989, 39(1): 201-225.

[24] J U Brackbill, D B Kothe, C A Zemach. Continuum method for modeling surface tension. *Journal of Computational Physics*, 1992, 100(2): 335-354.

[25] R L Hoffman. A study of the advancing interface. I. Interface shape in liquid-gas systems. *J. Colloid Interface Sci.*, 1975, 50: 228-241.

[26] Š Šikalo, H D Wilhelm, I Roisman, et al. Dynamic contact angle of spreading droplets: Experiments and simulations. *Phys. Fluids*, 2005, 17: 062103.

[27] I E Barton. Comparison of SIMPLE- and PISO-type algorithms for transient flows. *International Journal for Numerical Methods in Fluids*, 2015, 26(4): 459-483.

[28] K P Travis, K E Gubbins. Poiseuille flow of Lennard-Jones fluids in narrow slit pores. *The Journal of Chemical Physics*, 2000, 112(4): 1984-1994.

[29] L Klotz, A M Pavlenko, J E Wesfreid. Experimental measurements in plane Couette–Poiseuille flow: dynamics of the large-and small-scale flow. *Journal of Fluid Mechanics*, 2021, 912: A24.

[30] B Ryningen, P Tetlie, S G Johnsen, et al. Capillary forces as a limiting factor for sawing of ultrathin silicon wafers by diamond multi-wire saw. *Engineering Science and Technology*, 2020, 23(5): 1100-1108.